

## A CLUSTER OF GALAXIES HIDING BEHIND M31: XMM-NEWTON OBSERVATIONS OF RXJ0046.4+4204

OLEG KOTOV<sup>1,2,3</sup>, SERGEY TRUDOLYUBOV<sup>1,2,4</sup>, AND W. THOMAS VESTRAND<sup>1</sup>  
*The Astrophysical Journal, accepted*

### ABSTRACT

We report on our serendipitous discovery with the XMM-Newton Observatory of a luminous X-ray emitting cluster of galaxies that is located behind the Andromeda galaxy (M31). X-ray emission from the cluster was detected previously by ROSAT, and cataloged as RX J0046.4+4204, but it was not recognized as a galaxy cluster. The much greater sensitivity of our XMM-Newton observations revealed diffuse x-ray emission that extends at least 5' and has a surface brightness profile that is well fit by the  $\alpha$ - $\beta$  model with  $\beta = 0.70 \pm 0.08$ , a core radius  $r_c = 56'' \pm 16''$ , and  $\alpha = 1.54 \pm 0.25$ . A joint global spectral fit of the EPIC/MOS1, MOS2, and PN observations with Mewe-Kaastra-Liedahl plasma emission model gives a cluster temperature of  $5.5 \pm 0.5$  keV. The observed spectra also show high significance iron emission lines that yield a measured cluster redshift of  $z = 0.290$  with a 2% accuracy. For a cosmological model with  $H_0 = 71$  km s<sup>-1</sup> Mpc<sup>-1</sup>,  $\Omega_M = 0.3$  and  $\Omega_\Lambda = 0.7$  we derive a bolometric luminosity of  $L_x = (8.4 \pm 0.5) \times 10^{44}$  erg/s. This discovery of a cluster behind M31 demonstrates the utility of x-ray surveys for finding rich clusters of galaxies, even in directions of heavy optical extinction.

*Subject headings:* galaxies: clusters: Intergalactic medium - X-rays: observation - Cosmology

### 1. INTRODUCTION

Galaxy clusters are the largest gravitationally bound structures in the universe. The evolution of cluster number density of a given mass is sensitive to specific cosmological scenarios (e.g. Press & Schechter (1974)). So observations of galaxy clusters are an important tool for constraining fundamental cosmological parameters.

Due to the fact that 15% of the total cluster mass (e.g. Evrard (1997)) is in the form of hot diffuse plasma emitting at X-ray band via thermal bremsstrahlung (Sarazin 1988), galaxy clusters are among the most luminous objects in X-ray band. It makes X-ray selection an efficient means for constructing samples of galaxy clusters (see review by Rosati et al. (2002)). X-ray selection has the advantage that the measurable X-ray luminosity and temperature are correlated with the cluster mass.

Further, X-ray selection is useful for studying regions where optical searches are complicated because of dust extinction and heavy stellar confusion. X-rays are much less affected by extinction than optical photons and X-ray selection is almost free from source confusion problems (Ebeling et al. 2002). Conducting X-ray selection based on ROSAT data at low Galactic latitude, Ebeling et al. (2002) were able to detect 137 galaxy clusters, 70% of which were new discoveries.

With a new era of XMM-Newton and Chandra observatories with their large effective areas and wide energy ranges 0.3 – 10keV, the capability of X-ray selection increased. During an XMM-Newton observation of the galactic supernova remnant G21.5-09 located close to the Galactic Plane, Nevalainen et al. (2001) detected

a new galaxy cluster. Using only XMM-Newton data, they measured cluster redshift  $z = 0.1$  to 1% precision that is especially important in regions with such strong optical source confusion, where the optical redshift measurements of galaxies are difficult.

Here we present new XMM-Newton observations of the source RX J0046.4+4202 that indicate it is a high redshift cluster located behind M31. RX J0046.4+4204 was detected during the first and the second deep ROSAT RSPC surveys of M31 performed in June 1991 and July/August 1992 respectively (Supper et al. 2001). Based on a comparison of the first and the second surveys, RX J0046.4+4204 was classified as a potentially long term variable source. Our analysis of the data obtained with XMM-Newton revealed spatially extended emission, up to at least 5', from RX J0046.4+4204. The observed spectra show iron emission lines that yield a measured redshift of  $z = 0.290$  with a 2% accuracy. All these facts combined with optical image from Digitized Sky Survey allow us to conclude that RX J0046.4+4204 is actually a distant galaxy cluster.

In this paper, we assume the  $\Omega_M = 0.3$  and  $\Omega_\Lambda = 0.7$  cosmology with the Hubble constant of  $H_0 = 71$  km/s/Mpc. For the defined above cosmology and the measured redshift of  $z = 0.290$ , the angular size of 1' corresponds the physical size of 257 kpc. Statistical uncertainties are quoted at the 90% confidence level unless there is a statement saying otherwise.

### 2. OBSERVATIONS AND DATA REDUCTION

In the following analysis, we use the data from XMM-Newton observation of the XMM North 3 Field of M31 centered at RA =  $00^h46^m38^s.00$ ; Decl =  $+42^\circ16'20.0''$ . Fig. 1 (Left) shows optical image of M31 from Digitized Sky Survey with XMM-Newton FOV shown as a circle for M31 North 3 field. The XMM-Newton observation was performed on 2002 June 29 as a part of the Guaranteed Time Program (PI: K.O. Mason). An analysis of the complete North 3 field is presented in Trudolyubov

<sup>1</sup> NIS-2, Space and Remote Sciences Group, Los Alamos National Laboratory, Los Alamos, NM 87545

<sup>2</sup> Space Research Institute, Russian Academy of Sciences, Moscow, Russia

<sup>3</sup> Harvard-Smithsonian Center for Astrophysics, 60 Garden St., Cambridge, MA 02138

<sup>4</sup> Institute of Geophysics and Planetary Physics, University of California, Riverside, CA 92521

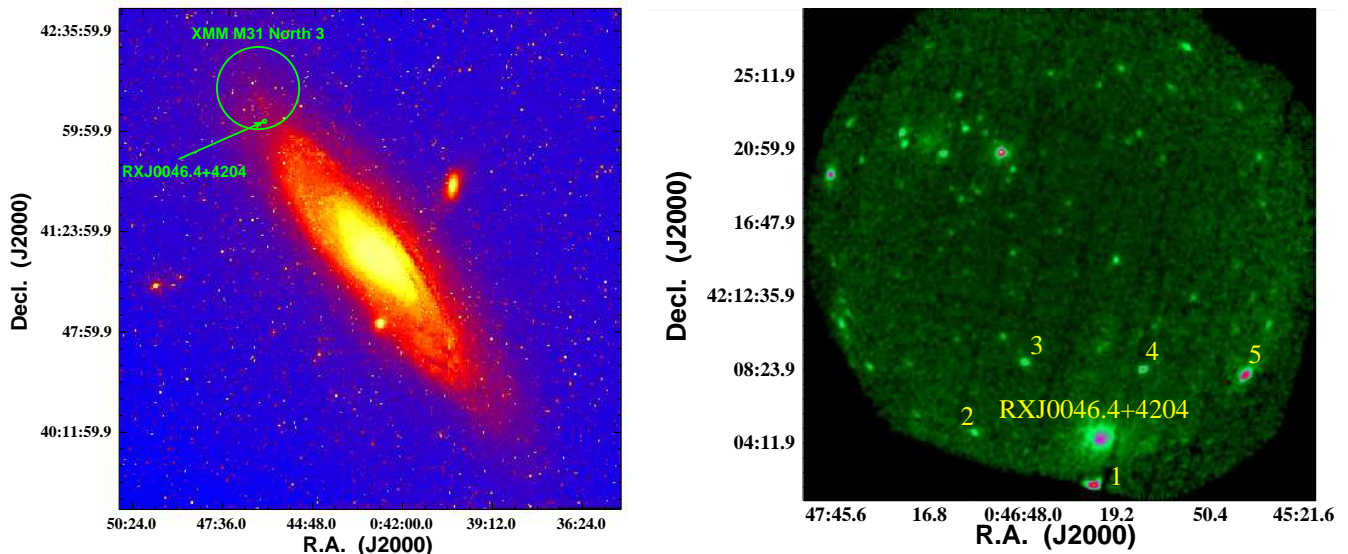


FIG. 1.— *Left*: Optical image of M31 from Digitized Sky Survey with XMM-Newton FOV show as a circle for M31 North 3 field. *Right*: The combined MOS1-MOS2-PN vignetting-corrected image of the XMM North 3 Field of M31 in 0.8 – 2.5 keV energy band, square root intensity scale.

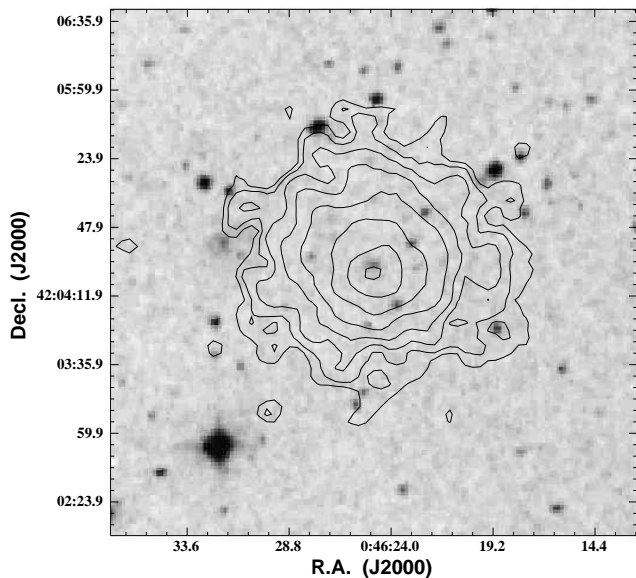


FIG. 2.— The Palomar Digitized Sky Survey optical image with overlaid brightness contours made from 0.8-2.5keV band MOS2/PN image. The X-ray image was smoothed with a  $4''$  Gaussian kernel. The contour levels are based on the background noise going up in logarithmic steps. MOS1 image was not used for construction of the contours because the center of the cluster falls at the edge of a CCD in MOS1 camera. The angular size of the largest contour corresponds to  $\sim 0.7$ Mpc at  $z = 0.29$ .

et al. (2005).

In current analysis, we used the data from two EPIC-MOS detectors (Turner et al. 2001) and the EPIC-PN detector (Strüder et al. 2001). The EPIC data was reduced using the standard *XMM-Newton* Science Analysis System (SAS v6.1.0)<sup>5</sup>. We used the calibration database with all updates available prior to January, 2005. Only X-ray events corresponding to patterns 0-12 for MOS detectors and patterns 0-4 for PN detector were selected. All known bad pixels were excluded.

<sup>5</sup> See [http://xmm.vilspa.esa.es/external/xmm\\_sw\\_cal/sas.shtml](http://xmm.vilspa.esa.es/external/xmm_sw_cal/sas.shtml)

The EPIC background is highly variable and only its quiescent component can be accurately modeled. To detect and exclude the periods of high flaring background, we produced the light curves for each EPIC detector showing count rate in the 2.0-15.0keV energy band from the whole field of view but with detected sources masked. The light curves were binned to 200 s time resolution. We screened the EPIC data to recursively exclude time intervals with the deviation of the count rate exceeding a  $2\sigma$  threshold from the average. Experiments with different choices of energy bands and flare detection thresholds have shown that our choice was close to optimal. The remaining good exposure time was  $\sim 24$  ks for the EPIC-PN,  $\sim 41$  ks for the EPIC-MOS1, and  $\sim 43$  ks for the EPIC-MOS2.

To account for strong *XMM* mirror vignetting, we used an approach proposed by Arnaud et al. (2001). Each photon was assigned a weight proportional to inverse vignetting and these weights were then used in computing images and spectra. This was done using the SAS tool *evigweight*.

Background modeling in our analysis was implemented following the double-subtraction method of Arnaud et al. (2002). The first step of this method is to subtract the particle-induced background component. This component can be estimated from a set of XMM observations with the filter wheel closed (so called “closed data”). We compiled the closed dataset from public observations available in the XMM data archive; these data were reduced following identical steps as the science observations. The closed background was adjusted to the cluster observations using the observed flux in the 10–15 keV band outside the field of view. The scaling factors are 1.04, 1.05, and 1.01 for MOS1, MOS2, and PN respectively. The second step is to determine the cosmic X-ray background (CXB) component. Its spatial distribution should be flat because vignetting correction is already applied. Therefore, the CXB component can be measured in the source-free regions of the field of view at large radii from the cluster center (see § 3.1 and 3.2 below).

TABLE 1  
RESULTS OF SPATIAL ANALYSIS. COMBINED  
EPIC-PN, MOS1 AND MOS2 DATA, 0.8 – 2.5  
keV ENERGY RANGE. PARAMETER ERRORS  
QUOTED ARE 90% CONFIDENCE LIMITS .

Parameters	$\beta$ fit	$\alpha - \beta$ fit
$\alpha$	...	$1.54 \pm 0.25$
$\beta$	$0.60 \pm 0.03$	$0.70 \pm 0.08$
$r_c$ (")	$20.2 \pm 2.8$	$56 \pm 16$
$r_c$ (kpc for $z=0.290$ )	$87 \pm 12$	$240 \pm 69$
$\chi^2/\text{dof}$	156.7(119)	139.4(118)

Finally, we applied a correction for photons registered during the CCD readouts, so called out-of-time events, to the EPIC-PN data.

### 3. RESULTS

The combined MOS1, MOS2, and PN image of the XMM North 3 Field of M31 in the 0.8 – 2.5 keV energy band, corrected for the effects of instrumental vignetting, is shown in Figure 1 (*Right*). The raw image was convolved with a Gaussian function with spatial scale  $\sigma = 4''$ . We define the cluster center to be at the location of the X-ray surface brightness peak of the cluster emission in the 0.8 – 2.5 keV energy band,  $\alpha = 00^h46^m24^s.8$   $\delta = +42^\circ04'26''$  (J 2000), with an estimated uncertainty radius of  $6''$  (90% CL), determined by the wavelet decomposition algorithm of Vikhlinin et al. (1998). The Palomar Digitized Sky Survey optical image shows no extended optical counterpart for RX J0046.4+4204 (see Fig. 2).

During the following spectral and spatial analysis, we excluded all detectable point sources from the data. The sources were detected separately in the “optimal” 0.3-3 keV, “soft” 0.3-0.8 keV, and “hard” 2.0-6.0 keV energy bands using the task *wdecomp* of the ZHTOOLS package<sup>6</sup>. Detected point sources were masked with circles of 80% PSF power radii.

#### 3.1. Spatial Analysis

Spatial analysis of the cluster emission was performed in the 0.8 – 2.5 keV energy band using all detectors. Experiments with different energy bands showed that the signal to noise ratio was close to optimal for the chosen band. We used a pixel size of  $4''$  in our spatial analysis. The image for each camera was corrected for vignetting. The PN image was corrected for out-of-time events. We subtracted the particle background component from the images as described in § 2.

We extracted the azimuthally averaged surface brightness profiles centered on the X-ray surface brightness peak, excluding the CCD gaps and circles around the point sources. The profiles were logarithmically binned with a step of  $\Delta r = 0.1r$ . A logarithmic radial binning approximately preserves the signal to noise ratio in annuli until the background becomes comparable to the signal. For the extracted profiles, the chosen step keeps the signal to noise ratio above 3 in annuli until  $\sim 5'$ . The obtained profiles were used to derive the parameters of

the spatial distribution of the ICM, cluster fluxes, and the level of the CXB component.

The cluster surface brightness profiles are often modeled with the so called  $\beta$ -model,  $n_e^2 \propto (1 + r^2/r_c^2)^{-3\beta}$  or  $S_x \propto (1 + r^2/r_c^2)^{-3\beta+0.5}$  (Cavaliere & Fusco-Femiano 1976). However, this model poorly describes clusters with sharply peaked surface brightness profiles related to the radiative cooling of the ICM in the cluster centers.

We used the simple modification of the  $\beta$ -model

$$n_e^2 \propto \frac{(r/r_c)^{-\alpha}}{(1 + r^2/r_c^2)^{3\beta-\alpha/2}}, \quad (1)$$

which allows to model a power law-type emission excess in the cluster centers. The similar models were also used by Pratt & Arnaud (2002) and Vikhlinin et al. (2005).

The model for the observed surface brightness profiles can be obtained by numerical integration of eq.(1) along the line of sight, and convolution of the result with the XMM PSF<sup>7</sup>. To represent the uniform sky X-ray background, we added a constant component to the model and treated it as a free parameter. The values of  $\alpha$ ,  $\beta$ , and  $r_c$  were derived from the joint fit to the observed profiles in the MOS1,2 and PN cameras, with the overall normalizations and background levels fit independently for each camera. The obtained parameters for the  $\alpha$ - $\beta$  model are summarized in Table 1.

We obtained a  $\beta$  value of  $0.70 \pm 0.08$ . For a sample of local clusters, Vikhlinin et al. (1999) showed that if cooling flow regions were excluded from  $\beta$ -model fit, values of the  $\beta$  parameter were distributed over a narrow range  $0.7 \pm 0.1$ . So the value of the  $\beta$  parameter we derived describes the typical distribution of the ICM.

The obtained value of the core radius,  $r_c = (56 \pm 16)''$  ( $(240 \pm 69)$  kpc for  $z=0.290$ ), is similar to the values of the  $r_c$  parameter Vikhlinin et al. (1999) measured for a sample of local clusters.

For the value of  $\alpha$  parameter we obtained  $\alpha = 1.54 \pm 0.25$ . This value is consistent with values of the  $\alpha$  parameter Vikhlinin et al. (2005) derived for typical cooling-flow clusters using a sample of local clusters. Vikhlinin et al. (2005) in their analysis used *Chandra* data where the PSF is not an issue, so their measurements of  $\alpha$  parameter are more direct and do not depend on the quality of a PSF model as in our case.

While the EPIC-pn PSF is azimuthally symmetric and is well calibrated up to large offset angles in the 0.8-2.5 energy band (see Fig 1-6 in Kirsch (2005)), the EPIC-MOS PSF is less reliable and seems not azimuthally symmetric. The asymmetry is not currently modeled in the SAS calibration. To check how imperfect calibration of the EPIC-MOS PSF can influence the obtained result, we fitted the surface brightness profile of the cluster extracted from the EPIC-PN detector alone. The obtained best-fit values were within our statistical uncertainties.

We can quantify the strength of cooling flow calculating the fraction,  $f_{70\text{kpc}}$  of the count rate coming from a central region of 70kpc to the total count rate (Peres et al. 1998). This quantity exhibits large dispersion, but in general, clusters with massive cooling flows show  $f_{70\text{kpc}} > 15\%$  (Peres et al. 1998). For a typical non-cooling-flows cluster  $f_{70\text{kpc}} \sim 6\%$  (Markevitch

<sup>6</sup> See <http://hea-www.harvard.edu/~alexey/zhtools/>

<sup>7</sup> We used the latest available values of the King function parametrization of the MOS1, MOS2, PN PSF, see <http://xmm.vilspa.esa.es/docs/documents/CAL-TN-0018-2-4.pdf>

1998). We estimated the count rate coming from the 70kpc central region using the best fit  $\alpha$ - $\beta$  model. The total count rate was calculated integrating the observed surface brightness profile within 1.4Mpc radius. We obtained  $f_{70\text{kpc}} = 18\%$ .

The combined MOS1-MOS2-PN surface brightness profile along with the best fit  $\alpha$ - $\beta$  model are shown in Fig. 3. From Fig. 3 one can see how the XMM PSF can flatten a peaked profile. For comparison, we also fit the surface brightness profiles by the standard  $\beta$ -model setting  $\alpha = 0$ . The obtained parameters are summarized in Table 1.

### 3.2. Global Spectrum

For our spectral analysis, we used the screened vignetting-corrected data in the 0.5 – 10.0 keV energy band from all cameras. The spectra of the cluster were extracted from a circular region with angular radius of  $3.1'$  (0.8Mpc for  $z=0.290$ ) for all EPIC data. All detected contaminating point-like sources were excluded from the source and background extraction regions. We subtracted the particle background component from the images as described in § 2. To estimate the remaining CXB component, we extracted the spectra from a circular region with angular radius of  $9.0'$  centered at the on-axis position, but a part of the region falling into the  $9.65'$  (2.5Mpc for  $z=0.290$ ) circle centered at the cluster center was excluded. The response matrices and effective area files were generated by the standard SAS tasks. Because the data were previously vignetting corrected, the effective area files were created for the on-axis position using the routine *arfgen*. The response matrices were generated in the spectrum extraction region via *rmfgen*.

The source spectra were binned to have at least 30 counts in each spectral bin and fit in XSPEC 11.3.0 (Arnaud 1996) by the Mewe-Kaastra-Liedahl plasma emission model (Mewe et al. 1985). We used abundances from Anders & Grevesse (1989). Galactic photoelectric absorption was accounted for using the WABS model (Morrison & McCammon 1983). The spectra from the EPIC-PN (3677 counts), MOS1 (1666 counts) and MOS2 (2179 counts) detectors were fitted both jointly and separately. For the joint fits, only spectral model normalizations were allowed to vary independently. The results of both joint and separate spectral fitting of the EPIC-PN, MOS1 and MOS2 data are summarized in Table 2.

We obtained a redshift value of 0.290 with 2% accuracy. The redshift values estimated independently from EPIC-PN, MOS1 and MOS2 data are in good agreement within measurement errors. For the value of hydrogen column density we obtained  $N_H = (2.2 \pm_{0.2}^{0.2}) \times 10^{21} \text{ cm}^{-2}$  that is significantly above the Galactic hydrogen column in the direction of M31,  $\sim 7 \times 10^{20} \text{ cm}^{-2}$  (Dickey & Lockman 1990). We checked that the values of absorption obtained independently from EPIC-PN, MOS1 and MOS2 data are consistent within the measurement errors.

The EPIC-PN, MOS1 and MOS2 spectra, along with the best-fit spectral models, are shown in Figure 4. Note that separate spectral fitting of the EPIC-PN, MOS1 and MOS2 data gives consistent values of the model parameters.

### 3.3. Temperature profile

To construct temperature profile, we extracted individual spectra in 5 annuli: 0 – 50kpc, 50 – 100kpc, 100 – 200kpc, 200 – 400kpc, and 800 – 1600kpc, centered on the position of the X-ray surface brightness peak using data from all cameras. After background subtraction, the number of counts (MOS1+MOS2+PN) in 0.5-10keV energy band in 1, 2, 3, 4, and 5 annuli was 632, 1275, 2071, 2069, 1063, and 459 accordingly.

The correction for the XMM PSF effect was done using an approach of Pointecouteau et al. (2004). Using the best-fit  $\alpha$ - $\beta$  models of the cluster brightness and the XMM PSF calibration, we calculated the redistribution matrix,  $R_{ij}$ , of each temperature to each annulus which represents relative contribution of emission from annulus  $i$  to the observed flux in annulus  $j$ . The model spectrum,  $S_j$ , is then given by

$$S_j = \sum R_{ij} S(T_i), \quad (2)$$

where  $T_i$  is the temperature in annulus  $i$  and  $S(T_i)$  is the *mekal* spectrum for this temperature. Fitting this model to the observed spectra in all annuli simultaneously and treating all  $T_i$  as free parameters gives the deconvolved temperature profile. Unfortunately, the statistic was poor to measure metallicity profile. So for all annuli we fixed the metallicity values at the best-fit values obtained from the global spectrum. We checked that allowing the absorption and the metallicity to be freely fitted does not significantly change the result. The values of redshift and absorption values were also fixed at the best-fit values.

We fitted the observed temperature profiles by a 3-D temperature model :

$$T(r) = T_0 / (1. + (x/0.6)^2)^\gamma, \quad (3)$$

where  $x = r/r_0$ . A similar model describes the temperature profiles for low redshift clusters (Vikhlinin et al. 2005). For local clusters,  $r_0$  scales with the cluster temperature as  $r_0 \simeq 0.50 T^{1/2}$  Mpc where  $T$  is in keV (see Fig. 16 in Vikhlinin et al. (2005)). For the best-fit temperature of  $T = 5.5\text{keV}$  derived from the global spectrum,  $r_0 = 1.17\text{keV}$ . We fixed  $r_0$  at the value suggested by the low redshift clusters only with an additional redshift scaling  $r_0 \propto 1/E(z)$ , where  $E(z) = \sqrt{\Omega_M(z+1)^3 + \Omega_\Lambda}$ , to account for the redshift dependence of the virial radius for clusters with a fixed temperature (Bryan & Norman 1998). To fit the observed profiles, we projected the 3-D model along the line of sight using the emission measure profile from the best fit  $\alpha$ - $\beta$  model. Projection was based on a weighting method which correctly predicts the best-fit spectral  $T$  for a mixture of different temperature components (Mazzotta et al. 2004; Vikhlinin 2005).

Our 3-D model has a flat shape in the central region ( $r < 0.6r_0/\gamma^{0.5}$ ) and is not intended for modeling central temperature drops associated with a cooling region. The innermost bin shows an apparent temperature drop and can indicate the presence of a cooling flow. Therefore we excluded the central bin from the fit. Taking into account the fact that the temperature profile was corrected for the XMM PSF this procedure is correct. The obtained best-fit model, the deconvolved and original temperature profiles are shown in Fig. 5. The uncertainties on the best-fit model were calculated from Monte-Carlo simulations.

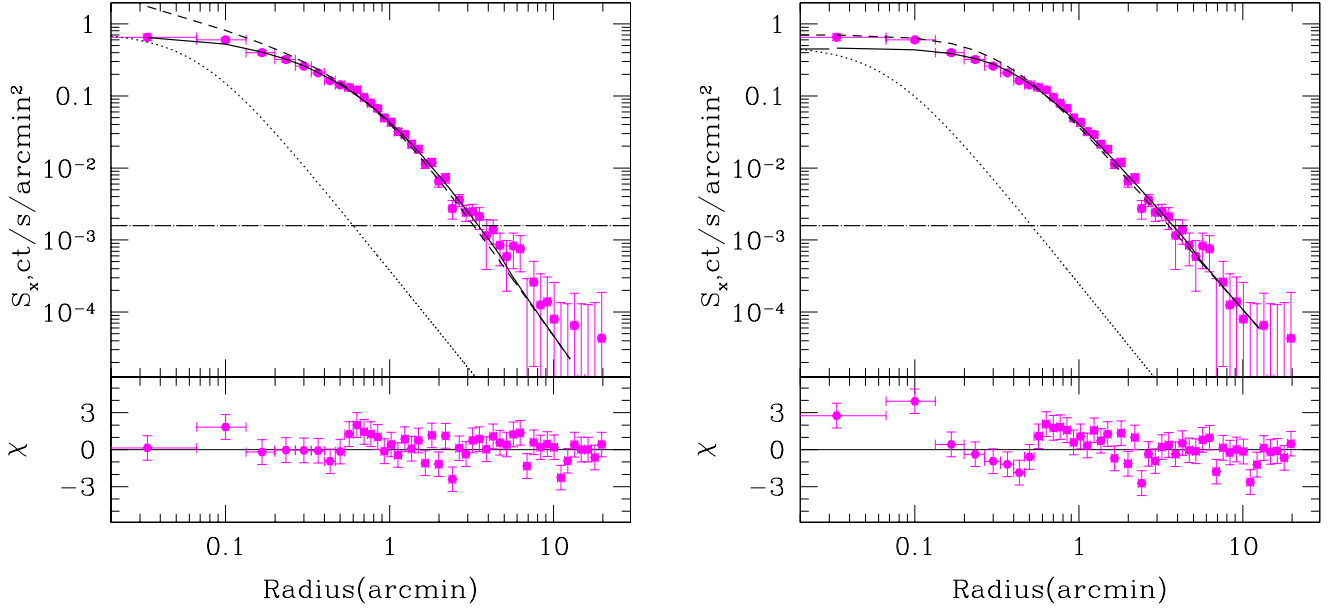


FIG. 3.— *Left*: Upper panel: The combined MOS1-MOS2-PN surface brightness profile of RX J0046.4+4204 in the 0.8 – 2.5 keV energy band. Black solid line shows  $\alpha$ - $\beta$  model best fit convolved with the XMM PSF. Black dashed line shows  $\alpha$ - $\beta$  model best fit. Black dotted line shows the XMM PSF. Black dotted-dashed line shows the level of the cosmic X-ray background component. Lower panel: The residual between the data and the best-fit model in terms of sigmas. *Right*: The same with the standard  $\beta$ -model best fit.

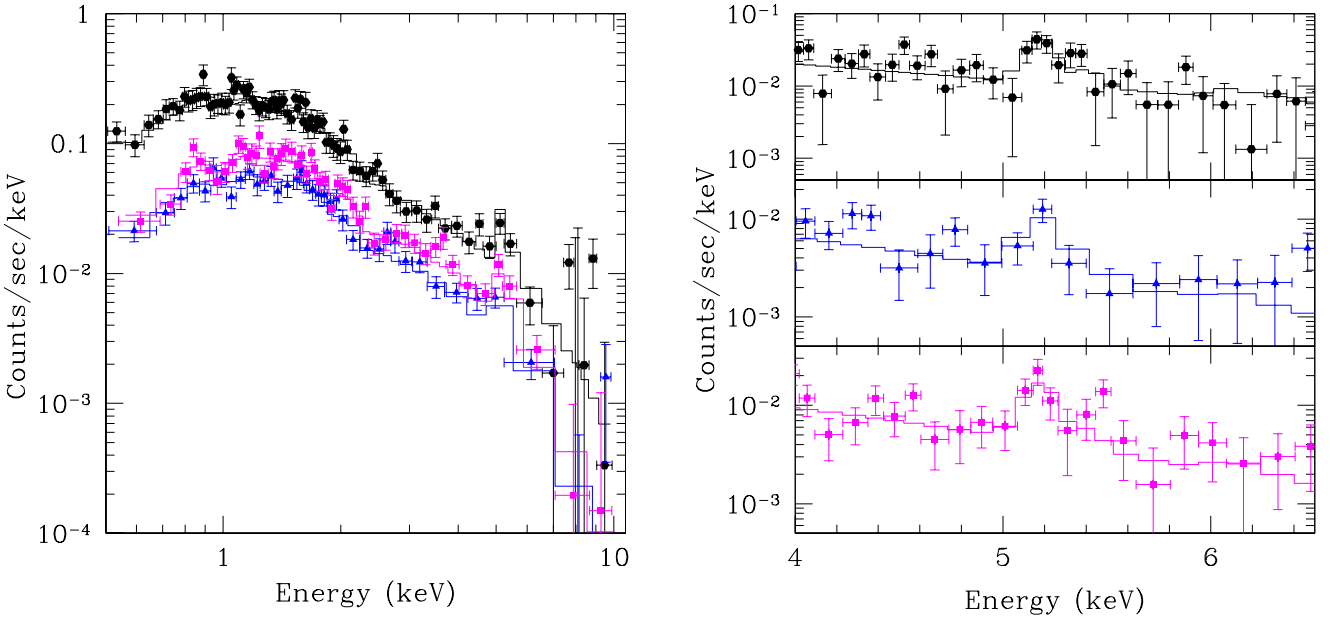


FIG. 4.— *Left*: Count spectra of RX J0046.4+4204 taken with the *XMM-Newton*/EPIC-PN (black circles), MOS1 (blue triangles) and MOS2 detectors (magenta squares). The corresponding best-fit spectral models (absorbed red-shifted *Mekal* model) convolved with instrumental responses are shown as black, red and blue solid lines. *Right*: Expanded view of the 4.0-7.0keV energy band. Upper, Middle and Lower panels show PN, MOS1 and MOS2 data. A red-shifted iron emission line feature is clearly evident.

We applied Gaussian scatter to the observed temperature profile within its uncertainties and fitted simulated profiles. The best-fit model uncertainties estimated as *rms* scatters in narrow radial bins from 1000 simulations are shown in Fig. 5..

### 3.4. Mass and Luminosity measurements

Assuming hydrostatic equilibrium for the ICM, we can use the best fit temperature and density profiles to derive the total cluster masses:

$$M(r) = -\frac{rT(r)}{G\mu m_p} \left( \frac{d \log \rho(r)}{d \log r} + \frac{d \log T(r)}{d \log r} \right) \quad (4)$$

We calculated the total mass of  $M_{500} = (5.1 \pm 1.1) \times$

TABLE 2  
RESULTS OF SPECTRAL ANALYSIS. EPIC-PN, MOS1 AND MOS2 DATA,  
0.5 – 10.0 keV ENERGY RANGE. SPECTRAL EXTRACTION RADIUS IS 3.1'.  
PARAMETER ERRORS QUOTED ARE 90% CONFIDENCE LIMITS .

Parameters	MOS1	MOS2	PN	Combined
$N_H(10^{22} \text{ cm}^{-2})$	$0.21 \pm 0.04$ $0.03$	$0.26 \pm 0.03$ $0.03$	$0.21 \pm 0.02$ $0.02$	$0.22 \pm 0.02$ $0.02$
$kT(\text{keV})$	$6.4 \pm 1.4$ $0.7$	$5.3 \pm 0.8$ $0.20$	$5.1 \pm 0.7$ $0.21$	$5.5 \pm 0.5$ $0.15$
$Z_\odot$	$0.44 \pm 0.19$ $0.27$	$0.72 \pm 0.19$ $0.20$	$0.45 \pm 0.10$ $0.21$	$0.57 \pm 0.13$ $0.13$
$z$	$0.296 \pm 0.011$ $0.023$	$0.292 \pm 0.009$ $0.007$	$0.287 \pm 0.008$ $0.008$	$0.290 \pm 0.005$ $0.005$

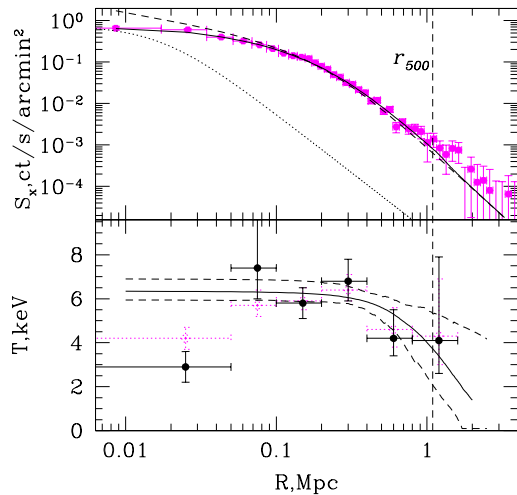


FIG. 5.— Upper panel: Same as Fig. 3 (Left upper panel). Lower panel: The temperature profile of the cluster as a function of angular radius obtained from EPIC-PN/MOS1/MOS2 data. Solid black circles show the deconvolved projected temperature profile. For comparison, open circles shows the raw measurement from the X-ray fit in the same annuli. The error bars correspond to 68% (1- $\sigma$ ) confidence limits. Solid line shows the best-fit projected temperature profile and dashed lines correspond to its 68% CL uncertainties.

$10^{14} M_\odot$  and the radius of  $r_{500} = 1.09 \pm 0.08 \text{ Mpc}$  corresponding to the mean overdensity  $\Delta = 500$  relative to the critical density at the cluster redshift. The uncertainties on the total mass due to the temperature profile were calculated analogically to the uncertainties on the best-fit temperature profile model. We calculated the total mass for each simulated profile. Then the uncertainties were calculated as the boundaries of the region containing 90% of all realizations. The total mass uncertainties due to the error on the density gradient were calculated following Pratt & Arnaud (2002). The value of  $d \log \rho(r)/d \log r$  at  $r_{500}$  was considered as an independent parameter of the  $\alpha$ - $\beta$  model instead of  $\beta$ . We refit the surface brightness profile with the new parameter set and measured the uncertainties on  $d \log \rho(r)/d \log r$  at  $r_{500}$ . The final total mass uncertainties were calculated by adding quadratically the total mass error due to the temperature profile and the density profile. The uncertainties on  $R_{500}$  are related to the total mass uncertainties as  $\sigma_{M_{500}}/M_{500} = 3\sigma_{r_{500}}/r_{500}$ .

We calculated the emission measure-weighted temperatures (volume-averaged with weight  $w = \rho_j^2$ ) of  $T_{emw} = 6.0 \pm 0.7$  within  $70 \text{ kpc} < r < r_{500}$ . It is not a surprise

that obtained  $T_{emw}$  is higher than the best-fit spectroscopic temperature because we excluded the innermost bin from the temperature profile fit. The uncertainties for  $T_{emw}$  were calculated from Monte-Carlo simulations in the similar way as for the temperature profile best-fit.

We can compare the obtained  $M_{500}$  with predicted value from  $M - T$  relations. We will use as a low-redshift reference the  $M - T$  relation from Vikhlinin et al. (2005), which is similar to the  $M - T$  relation measured by Arnaud et al. (2005). The  $M - T$  relation derived by Vikhlinin et al. (2005) predicts  $M_{500} = 6.1 \times 10^{14} M_\odot$  for a 6 keV cluster. The self-similar theory predicts that for the same temperature the mass evolves as  $M_\Delta \propto E(z)^{-1}$  with  $z$ , where  $E(z) = H(z)/H_0 = (0.3(1+z)^3 + 0.7)^{1/2}$  (e.g. Bryan & Norman (1998)). Dividing the predicted mass by  $E(z = 0.29)$  to place it at  $z = 0.29$ , we obtain  $M_{500} = 5.3 \times 10^{14} M_\odot$ . This value is in agreement with the derived  $M_{500} = (5.1 \pm 1.0) \times 10^{14} M_\odot$ .

We derived the unabsorbed bolometric luminosity of  $L_x = (8.4 \pm 0.5) \times 10^{44} h_{71}^{-2} \text{ erg s}^{-1}$  using the Mewe-Kaastra-Liedahl plasma emission model. We used  $T_{emw}$  as the temperature parameter for the model. The model was normalized by the following count rate: we subtracted from the observed 0.8 – 2.5 keV count rate calculated within  $0 < r < 1.4 \text{ Mpc}$  the count rate calculated from the best-fit  $\alpha$ - $\beta$  model within  $r < 70 \text{ kpc}$ , and multiplied the result by 1.06 (Markevitch 1998).

The fact that our analysis is similar to the one done by Markevitch (1998) for low redshift clusters allows us to compare the obtained luminosity with the prediction from their  $L - T$  relation. The  $L - T$  relation derived by Markevitch (1998) predicts the luminosity of  $6.2 \times 10^{44} h_{71}^{-2} \text{ erg s}^{-1}$  for a 6 keV cluster. It is well below the derived luminosity. However, correcting the predicted luminosity for the evolution in  $L - T$  relation,  $L_z = (1+z)^{1.5} L_0$ , reported by Vikhlinin et al. (2002), we obtain  $9.2 \times 10^{44} h_{71}^{-2} \text{ erg s}^{-1}$ . This value is close to the observed one.

#### 4. DISCUSSION AND CONCLUSIONS

Our deep XMM-Newton observations of M31 have shown that RX J0046.4+4204 is not located in that galaxy, but rather is actually a distant cluster of galaxies. We found RX J0046.4+4204 has spatially extended X-ray emission and that the spectrum clearly shows a red-shifted iron emission line. Straightforward fitting of the iron line yields a cluster redshift of  $Z=0.290$  with 2% accuracy and that the redshift values estimated independently from EPIC-PN and MOS data are in good agreement within measurement errors.

The large scale spatial distribution of RX

J0046.4+4204 is well fit by the  $\alpha$ - $\beta$  model with  $\beta = 0.70 \pm 0.8$ , a core radius  $r_c = (56 \pm 16)''$  or  $r_c = (240 \pm 69)\text{kpc}$  for  $z=0.290$ , and  $\alpha = 1.54 \pm 0.25$ . The obtained values of  $\beta$  and  $r_c$  are consistent with the parameters of typical clusters (Vikhlinin et al. 1999). The derived  $\alpha$  agrees with values measured for cooling flow clusters (Vikhlinin et al. 2005).

The spatially integrated X-ray continuum is well fit by red-shifted ( $z=0.290$ ) Mewe-Kaastra-Liedahl plasma emission model with low energy photo-electric absorption. The best fitting global model for the joint PN, MOS1, and MOS2 measurements yields the parameters  $kT(\text{keV}) = 5.5 \pm 0.5$ , fractional solar abundance  $Z_\odot = 0.57 \pm_{0.13}^{0.15}$ , a redshift  $z = 0.290 \pm 0.005$ , and a column depth  $n_H = 2.2(\pm_{0.2}^{0.2}) \times 10^{21}\text{cm}^{-2}$ . This derived column depth is significantly larger than the Galactic hydrogen column in the direction of M31,  $\sim 7 \times 10^{20}\text{cm}^{-2}$  (Dickey & Lockman 1990).

It is interesting to compare the value of absorption obtained for the cluster with absorption for the nearby X-ray sources. Fig 1(*Right*) shows five bright X-ray sources lying in the direct vicinity of RXJ0046.4+4204 for which Trudolyubov et al. (2005) were able to measure column depth based on their X-ray spectra and to identify some of them. XMMU J004540.5+420806(source #5 in Fig. 1) was identified as a foreground star with the column depth of  $0.2 \times 10^{21}\text{cm}^{-2}$  (two sigma upper limit). XMMU J004648.0+420851(source #3) was identified as a background radio source with the column depth of  $(4.0 \pm_{5.0}^{1.0}) \times 10^{21}\text{cm}^{-2}$ . XMMU J004627.0+420151(source #1) was identified as a globular cluster source in M31. The derived column depth for this source was  $(1.3 \pm 0.1) \times 10^{21}\text{cm}^{-2}$ . The nature of two last sources, XMMU J004611.5+420826(source #4) and XMMU J004703.6+420449 (source #2), was unclear. Trudolyubov et al. (2005) proposed that these sources could be two AGN located in the background of M31. The derived column depths of XMMU J004611.5+420826 and XMMU J004703.6+420449 were  $(2.5 \pm 0.3) \times 10^{21}\text{cm}^{-2}$  and  $(2.3 \pm 0.6) \times 10^{21}\text{cm}^{-2}$ , respectively.

The absorption value of the background radio source is 2 times higher than the cluster absorption and most likely to be intrinsic. The column depth of the glob-

ular cluster candidate is smaller than that of the cluster. To explain this fact, it might be proposed that the globular cluster candidate is located in front of the disk of M31, while the cluster is obscured by the disk. On the other hand, XMMU J004611.5+420826 and XMMU J004703.6+420449 have column depths consistent with that of the cluster, suggesting that they could be also located in the background of M31, although it is unclear what fraction of the column depths is intrinsic. This interpretation is in general agreement with results of spectral fitting of a large sample of M31 globular cluster X-ray sources (Trudolyubov & Priedhorsky 2004). Trudolyubov & Priedhorsky (2004) found that globular cluster sources located in front of M31 disk have typical values of absorbing column in the range of  $(0.5 - 1.5) \times 10^{21}$ , while the sources located behind the disk or embedded into it show higher absorbing columns of  $(2 - 4) \times 10^{21}\text{cm}^{-2}$ .

The extracted temperature profile corrected for the XMM PSF shows the central temperature decline that confirms the indication of cooling flow presence from the spatial analysis. Using the spatially resolve temperature profile we derived  $R_{500} = 1.09 \pm 0.07\text{Mpc}$ ,  $M_{500} = (5.3 \pm 1.0) \times 10^{14}M_\odot$ , and  $T_{emw} = 6.0 \pm 0.7$  within  $R_{500}$ . The values of  $M_{500}$  corrected for the evolution and  $T_{emw}$  are in agreement with local  $M - T$  relations.

The study we have presented here shows the utility of sensitive X-ray observations for identifying and studying clusters of galaxies in directions where foreground confusion or heavy optical extinction makes optical selection complicated.

We thank A. Vikhlinin for extensive discussions and helpful comments. Also we'd like to thank the referee for providing useful suggestions. This paper is based in part on observations obtained with *XMM-Newton*, an ESA science mission with instruments and contributions directly funded by ESA Member States and the USA (NASA). This work was supported in part by NASA grant NAG5-12390 and by Internal Laboratory Directed Research and Development funding at Los Alamos National Laboratory.

## REFERENCES

- Arnaud, K., 1996, in *Astronomical Data Analysis Software and Systems V*, ASP Conference Series 101, ed. G. Jacoby & J. Barnes (San Francisco: ASP) 17
- Anders, E., & Grevesse, N. 1989, *Geochim. Cosmochim. Acta*, 53, 197
- Arnaud, M., Neumann, D.M., Aghanim, N., et al., 2001, *A&A*, 365, L80
- Arnaud, M., Majerowicz, S., Lumb, D., et al., 2002, *A&A*, 390, 27A
- Arnaud, M., Pointecouteau, E., & Pratt, G. W. 2005, *A&A*, submitted (astro-ph/0502210)
- Bryan, G. L., & Norman, M. L. 1998, *ApJ*, 495, 80
- Cavaliere, A., Fusco-Femiano, R., 1976, *A&A*, 49, 137
- Dickey, J. M. & Lockman, F. J. 1990, *ARA&A*, 28, 215
- Ebeling, H., Mullis, C. R., & Tully, R. B. 2002, *ApJ*, 580, 774
- Evrard, A. E. 1997, *MNRAS*, 292, 289
- Kirsch, M., 2005, EPIC Status of Calibration and Data Analysis, <http://xmm.vilspa.esa.es/docs/documents/CAL-TN-0018-2-4.pdf>
- Markevitch, M., 1998, *ApJ*, 504, 27
- Mazzotta, P., Rasia, E., Moscardini, L., & Tormen, G. 2004, *MNRAS*, 354, 10
- Mewe, R., Gronenschild, E. H. B. M., & van den Oord, G. H. J. 1985, *A&AS*, 62, 197
- Morrison, R., & McCammon, D. 1983, *ApJ*, 270, 119
- Nevalainen, J., Lumb, D., dos Santos, S., Siddiqui, H., Stewart, G., and Parmar, 2001, *A.N., A&A*, 374, 66-72
- Peres, C. B., Fabian, A. C., Edge, A. C., Allen, S. W., Johnstone, R. M., & White, D. A. 1998, *MNRAS*, 298, 416
- Pointecouteau, E., Arnaud, M., Kaastra, J., & de Plaa, J. 2004, *A&A*, 423, 33
- Pratt, G.W., Arnaud, M., 2002, *A&A*, 394, 375
- Press, W. H., & Schechter, P. 1974, *ApJ*, 187, 425
- Rosati, P., Borgani, S., & Norman, C. 2002, *ARA&A*, 40, 539
- Sarazin, C. L. 1988, *Cambridge Astrophysics Series*, Cambridge: Cambridge University Press, 1988,
- Supper, R., Hasinger, G., Lewin, W.H.G., et al., 2001, *A&A*, 373, 63
- Strüder, L., et al. 2001, *A&A*, 365, L1
- Trudolyubov, S., & Priedhorsky, W. 2004, *ApJ*, 616, 821
- Trudolyubov, S., Kotov, O., Priedhorsky, W., Cordova, F., & Mason, K. 2005, *ApJ*, 634, 314
- Turner, M. J. L., et al. 2001, *A&A*, 365, L27
- Vikhlinin, A., McNamara, B. R., Forman, W., Jones, C., Quintana, H., & Hornstrup, A. 1998, *ApJ*, 502, 558
- Vikhlinin, A., Forman, W., & Jones, C. 1999, *ApJ*, 525, 47
- Vikhlinin, A., VanSpeybroeck, L., Markevich, M. et al., 2002, *ApJ* 578, L107

Vikhlinin, A. 2005, ApJ, submitted, (astro-ph/0504098)  
Vikhlinin, A., Kravtsov, A., Forman, W., Jones, C., Markevitch,  
M., Murray, S. S., Van Speybroeck, L. 2005, ApJ, submitted,  
(astro-ph/0507092)